Mechanical Engineering ETDs

Engineering ETDs

2-9-2010

Bioagent defeat in shock driven gas flow

Mario L. Chavez

Follow this and additional works at: https://digitalrepository.unm.edu/me_etds
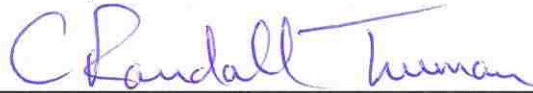
Mario L. Chavez

Candidate

Mechanical Engineering

Department

This thesis is approved, and it is acceptable in quality
and form for publication:

Approved by the Thesis Committee:

C Randall Truman ,Chairperson

Bioagent defeat
in
shock driven gas flow

by

Mario L. Chavez

B.S., Mechanical Engineering, University of New Mexico, 2004

THESIS

Submitted in Partial Fulfillment of the

Requirements for the Degree of

Master of Science
in
Mechanical Engineering

The University of New Mexico

Albuquerque, New Mexico

December, 2009

Dedication

To my parents, Louie and Yvonne, for their love, support, and encouragement.

"It's wonderful what we can do if we're always doing."

– George Washington

Acknowledgments

Bioagent defeat

in
shock driven gas flow

by

Mario L. Chavez

ABSTRACT OF THESIS

Submitted in Partial Fulfillment of the
Requirements for the Degree of

Master of Science

in

Mechanical Engineering

The University of New Mexico

Albuquerque, New Mexico

December, 2009

Bioagent defeat

in
shock driven gas flow

by

Mario L. Chavez

B.S., Mechanical Engineering, University of New Mexico, 2004

M.S., Mechanical Engineering, University of New Mexico, 2009

Abstract

The problem of planar shock interaction with gas cylinders whose axis of symmetry is parallel to the plane of the shock has been well studied both experimentally and numerically, and in this case, the flow evolution driven by Richtmyer-Meshkov instability is well characterized (although, as this thesis shows, assumptions commonly made about the experimental conditions need to be carefully checked). However, for a similar oblique interaction, with the plane of the shock and the axis of the density interface being non-parallel, presently only numerical results exist. The problem of oblique shock interaction is quite interesting to study experimentally both because of a variety of relevant applications and because it adds large-scale three-dimensionality to the initial conditions. Additionally, there is a considerable interest in the problem of shock interaction with particulates, droplets, and bioagents suspended in gas.

Here we describe an experimental arrangement for the studies of planar and oblique shocks and present some preliminary results.

Contents

Contents

List of Figures

List of Figures

List of Figures

Glossary

α	Thermal diffusivity
γ	Heat capacity ratio
η	Perturbation
θ	Temperature difference
λ	Wavelength
μ	Dynamic viscosity
ρ	Density
σ	Stress
τ	Time constant
A	Atwood number
Bi	Biot number
c	Speed of sound
c_p	Heat capacity at constant pressure
c_v	Heat capacity at constant volume
d	Diameter

Glossary

Fo	Fourier number
k	Wavenumber
M	Mach number
p	Pressure
r	Radius
R	Gas constant
t	Time
T	Temperature
v	Velocity
CFD	Computational fluid dynamics
DAQ	Data acquisition system
FEA	Finite element analysis
$LANL$	Los Alamos National Laboratories
PIV	Particle image velocimetry
$PLIF$	Planar laser induced fluorescence
RMI	Richtmyer-Meshkov Instability
RTI	Rayleigh-Taylor Instability
SF_6	Sulfur hexafluoride

Chapter 1

Introduction

1.1   Overview

Experimental study of shock wave physics is highly sought after to benchmark computational fluid dynamic (CFD) solvers used to analyze compressible flows in the high Mach number regime. This research and development effort is meant to experimentally quantify multiphase mixing flows. A shock tube facility has been designed and constructed, and is being used to study multiphase compressible flows. The usefulness of this facility includes the ability to produce quantitative benchmarking for numerical codes, by modeling flows that exist under more severe conditions. This facility is also well suited for direct studies of bioagent interactions with high speed flow. The physical phenomena involved in the shock driven transport of these particles may lead to bioagent defeat.

The goals are to gain a fundamental understanding of the physics of particulate and agent dynamics in multiphase shocked flow and turbulent mixing, advance the state of the art in diagnostic techniques, and investigate the possibility of attaining higher local Mach numbers in experiments via shock focusing. This understanding may lead to improved modeling and simulation by providing quantitative benchmark

data from well-characterized experiments describing multiple phenomena including shock propagation through multiphase media and the resulting gas and particle dynamics.

The Rayleigh-Taylor Instability (RTI) is the process of two fluids interacting across pressure and density gradients [1]. The Richtmyer-Meshkov Instability (RMI) characterizes a compressible fluid dynamic interaction of two gases with different densities under shock accelerated compression [2, 3]. The most elegant means of studying shock wave interactions is with a shock tube. With a tiltable shock tube facility the RMI phenomenon may be investigated under countless initial conditions. The need for this facility has been met by the development of a $5.8\ m$ long shock tube, which is housed in the Mechanical Engineering building at the University of New Mexico. This facility is being used to observe and analyze RMI on particles and droplets at various Mach numbers and with initial conditions influenced by tilt angle.

This shock tube does not have a predetermined fixed mounting angle, making it the first ever *tiltable* shock tube capable of safely producing shocks up to Mach 4. Interesting 3-phase flow phenomena are observed during high Mach number RMI investigations. These interactions are considered 3-phase since they include the mixing of particles with light and heavy gas. Shock wave behaviors are studied by constructing a shock tube with a transparent test section and instrumenting the tube with innovative diagnostic capabilities. Shock wave acceleration of a cylinder containing a mixture of heavy gas, sulfur hexafluoride (SF_6), seeded with droplets and or particles will be presented.

Ultra high-speed photography is used to capture images of a moving shock wave passing through a heavy gas cylinder containing particles and/or droplets. Current diagnostic capabilities include Mie scattering imaging, which allows the capture shock wave interactions using visible light. Under planar shock conditions, Mie scattering visualization of the top view revealed the onset of RMI with the onset of double

reverse vorticies. In the tilted 15° configuration, using Mie scattering, the top view only reveals the length of the heavy gas cylinder and requires alternative techniques to study oblique RMI. Once advanced capabilities such as planar laser induced fluorescence (PLIF) and particle image velocimetry (PIV) are incorporated, analysis of the high-speed images will allow in depth RMI investigations of any cross-section in the heavy gas cylinder, both in the planar and tilted configurations. Further studies of shock wave interaction with suspended particles will provide the desired benchmarks for computational codes.

The shock tube is tiltable, allowing the study of multiple shock angles with corresponding three-dimensional (3-D) RMI behaviors. The non-horizontal configuration is used to study oblique interaction. Experimenting with both horizontal and 15° shock angles produced images which provide evidence that shock waves are capable of combating suspended bioagents. These images provide important contributions to the development of computational simulation models, allowing the validation of CFD codes.

Bioagent Defeat Application

Fundamental understanding of shocked particle and droplet behavior is important for many problems related to bioterrorism. Bioterrorism can include the release of micro-organisms, or bioagents, in aerosol form. These bioagents may include bacterial spores, such as *bacillus anthracis* or lethal factor anthrax.

Anthrax spores germinate once attaching to a victim and cause sickness and death a number of different ways. Anthrax can be inhaled where it will germinate in the lungs, ingested into the digestive track where it causes upper gastrointestinal complications, and it can also attach to the outer body on open wounds [4]. Anthrax spores are protected by a tough protein coat of D-glutamate [5], making them difficult to defeat.

Shock waves traveling at high Mach numbers, those $\geq$ Mach 3, may combat potential airborne biological threats. Shock waves can rapidly change the environmental interface surrounding the bioagent. These environmental changes include rapid acceleration, high compression, heating, and RMI induced turbulent mixing. The tiltable shock tube leads to experimental studies of shock wave effects on airborne bioagents.

The effects that a shock wave has on aerosols in the flow include particle/droplet advection, clumping, and breakup. The shock tube facility will be used to investigate the lethality of shock waves against airborne biological components by demonstrating the effects of acceleration, heating, and the interface breakup on bacterial spores. This will lead to advancements in shock wave interactions to combat this threat.

1.2   Governing Equations

A basic shock tube apparatus is a long and straight tube divided into two main sections, the high pressure region or driver section and the low pressure region or driven section, as shown in Fig. 1.1. These two sections are separated by a removable diaphragm, which isolates two gases of differing pressure and/or density. When the diaphragm is removed or ruptured, a compression wave from the driver section enters the driven section, and the wave quickly steepens into a shock front. The shock wave travels through the driven section gas at supersonic velocity. The shock wave induces a flow of the driven gas which follows behind the shock at a lower velocity. This is know as the piston velocity of the flow. The driven gas experiences increased pressure, density, and temperature as the shock wave passes. Simultaneously, an expansion fan, also referred to as a rarefaction wave, travels back into the driver section, as shown in Fig. 1.1. The rarefaction wave reflects off the driver section end-cap and travels into the driven section, carrying the driver gas into the driven gas, as shown in Fig. 1.1; the line separating the two gases is the contact surface. When the
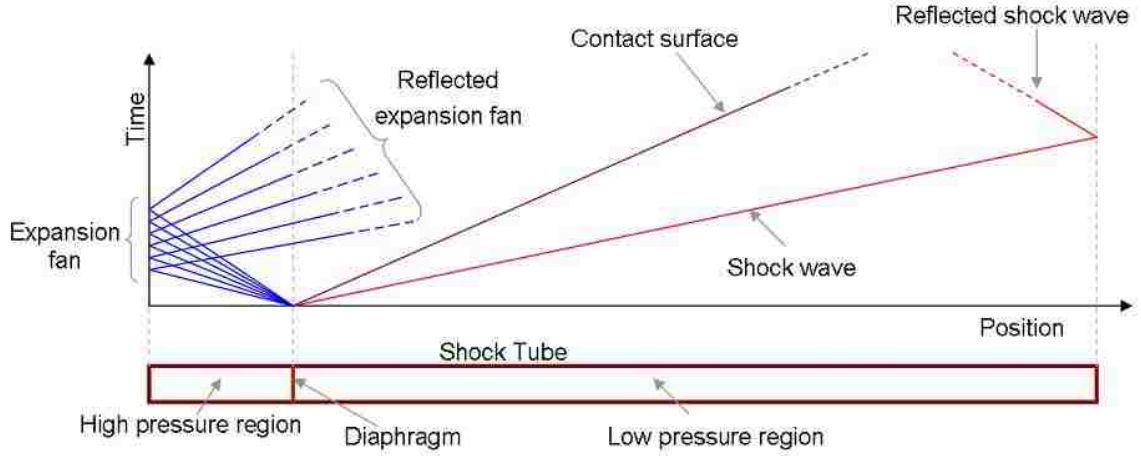
Figure 1.1: The waves formed in a shock tube upon diaphragm rupture.

shock wave reaches the end of the driver section it is reflected back into the flow and further increases the density, pressure, and temperature of the driven gas; this is referred to as shock focusing. Shock focusing allows for higher Mach numbers to be obtained. Through shock focusing the temperature and pressure are increased significantly but the effects are short lived. Microseconds after the the flow is shock focused the expansion fan arrives, cooling the gas and reducing the pressure.

A sound wave is a small pressure disturbance that propagates through a gas, liquid, or solid at a velocity, c, that depends on the properties of the medium. The speed of sound is an important property in the study of compressible flows [6]. Experiments indicate that the change in properties like pressure and density across a sound wave is nearly isentropic and the speed of sound in an ideal gas [6] is given by

$$c = \sqrt{\gamma R T} \tag{1.1}$$

where R is the gas constant, T is temperature. The heat capacity ratio is

$$\gamma \equiv \frac{c_p}{c_v} \tag{1.2}$$

where c_p is specific heat at constant pressure and c_v is specific heat at constant volume. The Mach number is the most important parameter in shock wave physics [7], defined as

$$M \equiv \frac{v}{c} \tag{1.3}$$

where v is the velocity of the medium. Both v and c are computed locally for conditions that actually exist at the same point [6]. If the velocity is less than the local speed of sound, M is less than 1 and the flow is called *subsonic*, and if the velocity is greater than the local speed of sound, M is greater than 1 and the flow is called *supersonic* [6].

Shock waves occur when discontinuities exist in a gas or fluid. Taylor developed a theory to characterize the growth of sinusoidal perturbations on an interface between a heavy fluid, of density ρ_2, over a light fluid, of density ρ_1, in a constant gravitation field using linear stability theory [1, 3, 8]. Given a perturbation of $\eta\left(x,t\right) = a\left(t\right)cos\left(kx\right)$ the perturbation amplitude grows according to

$$a = a_\circ cosh\left(\sqrt{kgAt}\right) \tag{1.4}$$

where $a_\circ$ is the initial perturbation amplitude, $k = 2\pi/\lambda$ is the wavenumber, and g is the acceleration due to gravity. The Atwood number is defined as the difference between fluid densities divided by their sum

$$A = \frac{\rho_2 - \rho_1}{\rho_2 + \rho_1}. \tag{1.5}$$

By convention the acceleration is directed from fluid 2 to fluid 1. Therefore, the Atwood number is positive if acceleration is directed from a heavy to a light fluid [8]. For example, the Atwood number for SF_6 and *air* is

$$A_{SF_6-air} = \frac{6.13 - 1.2}{6.13 + 1.2} \cong 0.673. \tag{1.6}$$

1.3   Prior Richtmyer-Meshkov Instability Studies

Numerous experiments have been conducted in the physics division of Los Alamos National Laboratory (LANL). Kumar et al. [9] conducted shock tube experiments to observe material stretching in shock-accelerated gaseous flows. The study focused on experimentally measuring the rate of interfacial area generation in shock-accelerated gaseous flows. A Mach 1.2 shock wave with Reynolds number $\approx 25,000$ was propagated downstream toward the test section. They conducted trials using five different configurations: Single-cylinder, Double-cylinder, Three-cylinder, Triple-cylinder with 1cyl-up, and Triple-cylinder 2cyl-up. The imaging technology was planar laser-induced fluorescence (PLIF). These images were used to measure the interfacial area growth rate. They concluded that the number, configuration, and orientation of gaseous cylinders affects shock-induced mixing. Comparison with simulations reveals agreement for single-cylinder and three cylinders, with one cylinder forward and two behind. Further investigations included late-time mixing, along with the effects of Mach number, cylinder diameter, and Atwood ratio. The ability to match these results elsewhere and including stronger shock waves could further this investigation.

Kumar et al. [10] sought to benchmark General Aerodynamic Simulation Program (GASP), a CFD code from AeroSoft Inc., Blacksburg, VA, for use in RMI simulations. The study investigates a density interface subjected to impulsive acceleration. A cylinder of heavy gas, sulfur hexafluoride, SF_6, was injected into a lighter gas, air. The SF_6 cylinder was accelerated by a planar shock wave traveling at Mach 1.2. This study concludes that the 2-D GASP simulation is consistent with experimental results. There is a need to investigate RMI with stronger shock waves.

Zhang et al. [11] numerically investigated vortex dynamics in baroclinically-forced inhomogeneous turbulence for shock wave interactions with heavy curtains. They present the main geometrical configurations and parameter space, and discuss the numerical scheme. They use a numerical model of a shock tube with a large aspect

ratio of 8 : 1 to study turbulence phenomena beyond intermediate times. They are interested in interactions during the transition to turbulence. Next, they discuss a simulation of a Mach 2.0 shock interaction with a SF_6 curtain and explain the phenomena and major physical processes. A negative vortex layer is deposited baroclinically on the upstream interface by the shock wave. The shock inside the curtain hits the downstream interface and deposits a positive vortex layer baroclinically, compressing the gas curtain. The gas curtain then deforms and splits into upstream and downstream jets with heavy gas residues left in the middle of the shock tube. The vorticity on the interface drives the deformation of the gas layer. The baroclinic term is the only physical source for the vorticity in the 2-D simulation. The baroclinically driven vortex bilayer and vortex projectile evolution are essentially the same regardless of the initial parameter. They then incline the numerical shock tube to study 3-D initial conditions, increasing the complexity dramatically. The vortex stretching term in 3-D dominantly contributes to the enstrophy production. The baroclinic term is not negligible in 3-D. They conclude by requiring more comprehensive understanding of the behavior of the baroclinic term in 3-D and await future investigation and experimental comparisons.

Comprehensive experimental benchmarks for numerical simulation software used to investigate RMI in the high shock regime remain unavailable. This issue is addressed with the construction of a new tiltable shock tube facility capable of capturing shock wave behavior up to Mach 4.0. This facility will also further the understanding of the baroclinc term present in 3-D initial conditions, through experimentation with the tiltable shock tube.

Presented next is a bioagent lethality study, followed by a description of the tiltable shock tube design, construction, and operation. Finally, preliminary experimental results of 2-D and 3-D shock interactions will be discussed. Many of the concepts and results presented in this thesis have been briefly described by Chavez, Vorobieff, Truman, and Johnson [12].

Chapter 2

Lethality Study

As a shock wave travels through a gas such as air, rapid changes in the density, pressure, and temperature occur behind the shock front. The shock wave will affect particle matter suspended in the low pressure section of the shock tube. Thus, there is an opportunity to use these effects to neutralize suspended bioagent material.

2.1 Theoretical Conditions Across the Shock

As stated in Chapter 1, the Mach number is the most important parameter in shock wave physics. Since the Mach number is local, there is one Mach number in front of the shock and another Mach number behind. The following equations are fundamental to the study of shock waves and particle interactions and require values for both M_1 and M_2 [7]. However, these values are related and M_2 can be written in terms of M_1 as

$$M_2^2 = \frac{2 + (\gamma - 1)\,M_1^2}{2\gamma M_1^2 - (\gamma - 1)} \tag{2.1}$$

where M_1 is the initial Mach number, M_2 is the Mach number behind the shock wave and γ is the heat capacity ratio. This relation is used for calculating the gas

property changes associated with shock wave physics.

The density of gas rises behind the passage of a shock wave [6]. The density ratio across the shock wave is

$$\frac{\rho_2}{\rho_1} = \frac{(\gamma + 1) M_1^2}{(\gamma - 1) M_1^2 + 2} \tag{2.2}$$

where ρ_1 is initial gas density and ρ_2 is the gas density behind the shock wave. This density rise is the direct result of gas compression [7]. As the Mach number increases the density ratio also increases at a decreasing rate as shown in Fig. 2.1. A density increase in the air surrounding bioagents could cause clumping where the
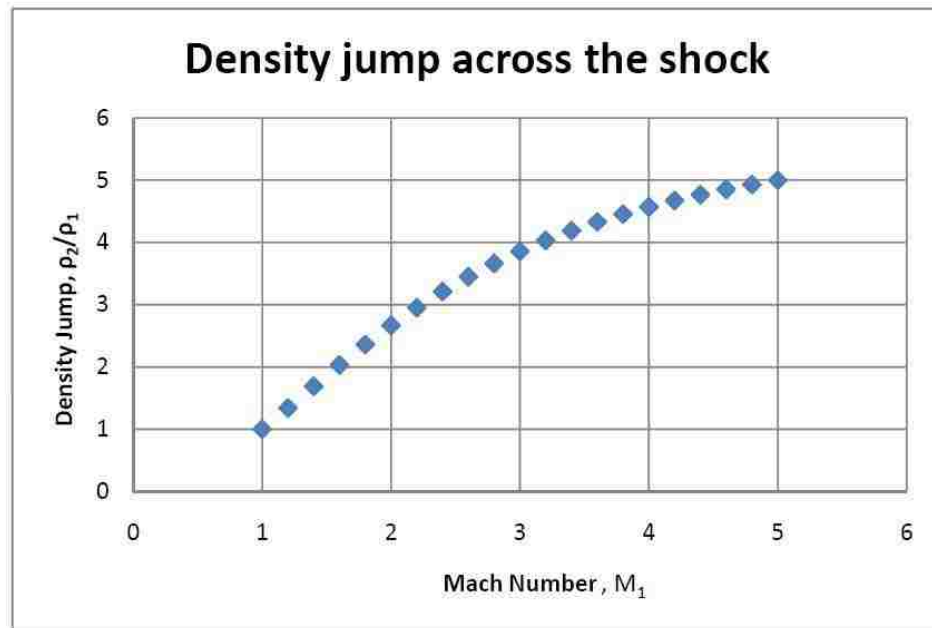
Figure 2.1: The density ratio across a normal shock vs. Mach number in a polytropic gas with $\gamma = 1.4$.

mass of a suspended particle is initially negligible, but the mass of many particles being compressed together may begin to affect suspension. The clumped collection of bioagents may fall to the ground, reducing the chances of human ingestion.

There is also a pressure rise across the shock wave [6]. The pressure ratio is

$$\frac{p_2}{p_1} = \frac{2\gamma}{\gamma+1}M_1^2 - \frac{\gamma-1}{\gamma+1} \tag{2.3}$$

where p_1 is initial pressure and p_2 is the pressure behind the shock wave. This pressure rise is shown in Fig. 2.2. The pressure jump is an increasing function where pressures increase more as the initial Mach number is increased. The pressurization of gas surrounding bioagents may cause the particle to be compressed and the particle to accelerate in the direction of the shock wave. The compression of the bioagent may lead to implosion of the particle but the compression characteristics of these particles is not yet understood.
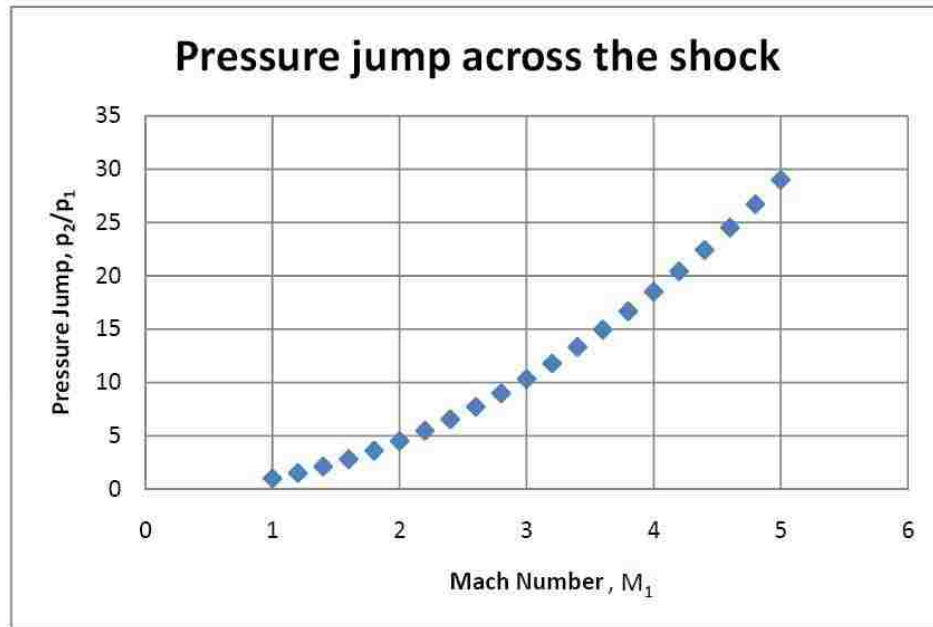
Figure 2.2: The pressure ratio across a normal shock vs. Mach number in a polytropic gas with $\gamma = 1.4$.

Rapid temperature rise is also associated with shock wave passage [7]. The temperature ratio across the shock wave is

$$\frac{T_2}{T_1} = \frac{[2\gamma M_1^2 - (\gamma-1)]\,[(\gamma-1)\,M_1^2 + 2]}{(\gamma+1)^2\,M_1^2} \tag{2.4}$$

where T_1 is the initial temperature of the gas and T_2 is the temperature of the gas behind the shock wave. As shown in Fig. 2.3, the rate of temperature rise behind the shock wave increases as the Mach number is increased. The heating of the gas
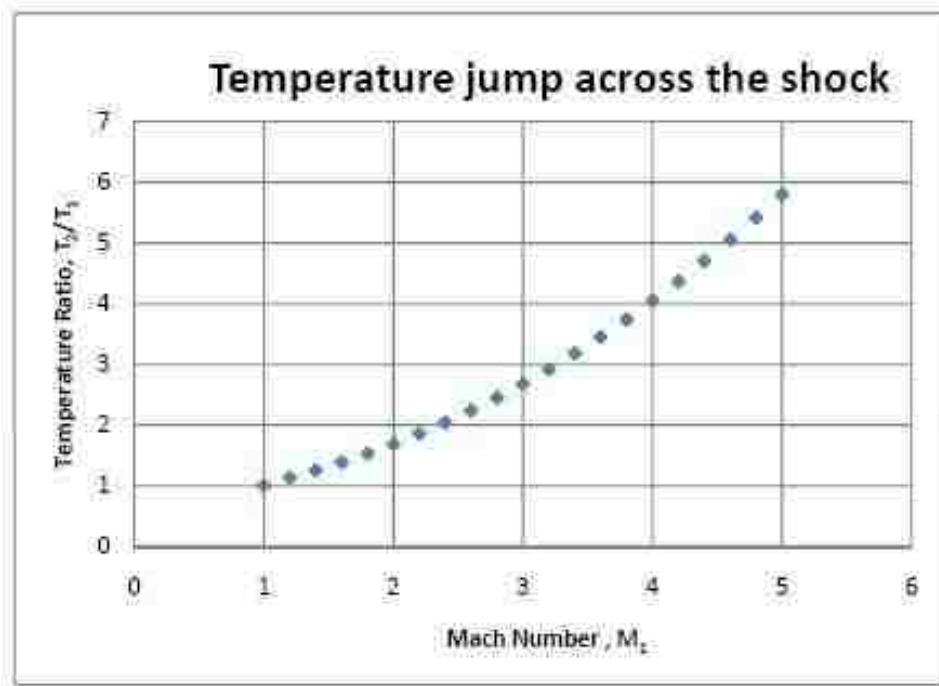
Figure 2.3: The temperature ratio in a polytropic gas with $\gamma = 1.4$.

will cause the temperature of suspended particles to increase. Transient heat transfer from the gas to the particles may neutralize bioagents, and will be discussed in Section 2.3. The temperature rise for very strong shock waves [7], in which $(\gamma - 1)\, p_2$ is very large compared with $(\gamma + 1)\, p_1$, is a limiting case described by

$$\frac{T_2}{T_1} = \frac{(\gamma - 1)\, p_2}{(\gamma + 1)\, p_1}. \tag{2.5}$$

The ratio T_2/T_1 increases to infinity as p_2/p_1 grows infinitely large [7]. Thus, the temperature discontinuity in a shock wave, like the pressure discontinuity, can be arbitrarily large.

2.2   Instantaneous Acceleration Effects

Suspended particles are accelerated by the pressure rise and shock-induced gas flow. The piston velocity induced by the passage of the shock wave [7] is

$$v_2 = \left\{ \frac{1}{2} \frac{c_2^2}{\gamma} \left[\gamma - 1 + \frac{(\gamma + 1)\, p_1}{p_2} \right] \right\}^{1/2} = v_g \tag{2.6}$$

where c_2 is the local speed of sound behind the shock, and v_g is the gas velocity. Using the Stokes approximation for particles suspended in a viscous gas [13], the equation of motion is

$$\rho_p \frac{\pi}{6} d_p^3 \frac{dv_p}{dt} = -3\pi d_p \mu_g \left(v_p - v_g \right) \tag{2.7}$$

where μ_g, the dynamic viscosity of the gas, increases with temperature. The rate of change of momentum of the particle equals the drag force on the particle. If impulsive acceleration from rest is assumed, the particle velocity is

$$v_p = v_g \left[1 - exp \left(-\frac{t}{\tau_{rel}} \right) \right] \tag{2.8}$$

where τ is the Stokes relaxation time [13] of the particle

$$\tau_{rel} = \frac{\rho_p d_p^2}{18 \mu_g}. \tag{2.9}$$

Assumptions made about the non-gaseous phase include characteristic particle size, $d_p = 500\ nm$, and the particle density, $\rho = 998\ kg/m^3$. The acceleration effects are represented as a "lethality factor," as shown in Fig. 2.4. The lethality factor used here is the Stokes relaxation time by the average particle acceleration, $\tau_{rel} \times a_{avg}$. The dashed line represents a crash survived by race car driver Kenny Brack in 2003. Lethality factors much larger than this severe incident may indicate that bioagents could be destroyed by shocks with Mach numbers as small as 4.
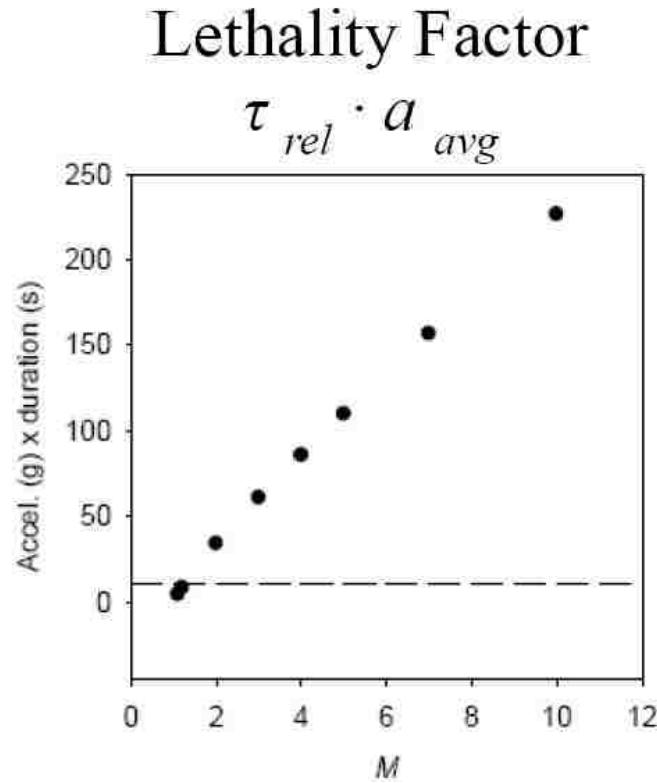
Figure 2.4: Shock acceleration lethality factor for a 500 *nm* particle at 99% piston velocity. The dashed line indicates a crash survived by race car driver Kenny Brack in 2003.

2.3   Transient Heating Effects

The rapid change in a particle's environment produces a transient heat transfer that may be used to defeat the threat from bioagents. The problem involves a temperature difference between the particle's initial temperature and the elevated temperature of its surroundings. Heat is transfered to the surface of the particle through convection and into its core through conduction. The convection coefficient is a local property that adjusts as the surface conditions change. The lumped capacitance method may be used when a particle has a Biot number much less than one [14]. The Biot number, Bi, is

$$Bi = \frac{hd_p}{k} < 0.1 \tag{2.10}$$

where h is the convection coefficient, k is the conduction coefficient, and d_p is the characteristic length, which in this case is the average diameter of the particle. The Biot number provides a measure of the temperature difference in the solid relative to the temperature difference between the surface and the fluid [14]. Conduction heat transfer inside the particle is taking place faster than convection to the particle.

By applying the lumped capacitance method, it is assumed the temperature of the solid is spatially uniform at any instance. The transient temperature response is determined by formulating an overall energy balance for the solid, which relates the rate of heat gain at the surface to the rate of change of the internal energy [14]. The initial temperature difference [14] between the particle and the post shock gas is

$$\theta_i \equiv T_i - T_\infty \tag{2.11}$$

where $T_i = T(0)$ is the initial temperature of the particle, and T_∞ is the temperature of the gas surrounding the particle. The temperature difference during heat transfer is

$$\theta \equiv T - T_\infty \tag{2.12}$$

where T is a function of time. The Fourier number, or the dimensionless time which characterizes heat conduction [14], is the ratio of the heat conduction rate to the rate of thermal energy storage. The Fourier number is

$$Fo \equiv \frac{\alpha t}{d_p^2} \tag{2.13}$$

where α is the thermal diffusivity of the particle and t is time. Using the Biot number and Fourier number, the temperature difference between the particle and its surroundings may be expressed as

$$\frac{\theta}{\theta_i} = \frac{T - T_\infty}{T_i - T_\infty} = exp\left(-Bi \cdot Fo\right). \tag{2.14}$$

The temperature increase in the gas leads to the heating of the particles. From Eq. 2.4, the temperature of the gas behind the shock is

$$T_\infty = T_2 = \frac{\left(1 + \frac{\gamma-1}{2}M_1^2\right)\left(\frac{2\gamma}{\gamma-1}M_1^2 - 1\right)}{\frac{(\gamma+1)^2}{2(\gamma-1)}M_1^2}T_1. \tag{2.15}$$

An analysis of the temperature rise of particles suspended in air, due to shock wave passage, is presented in Fig. 2.5. The solid curve in Fig. 2.5 represents the
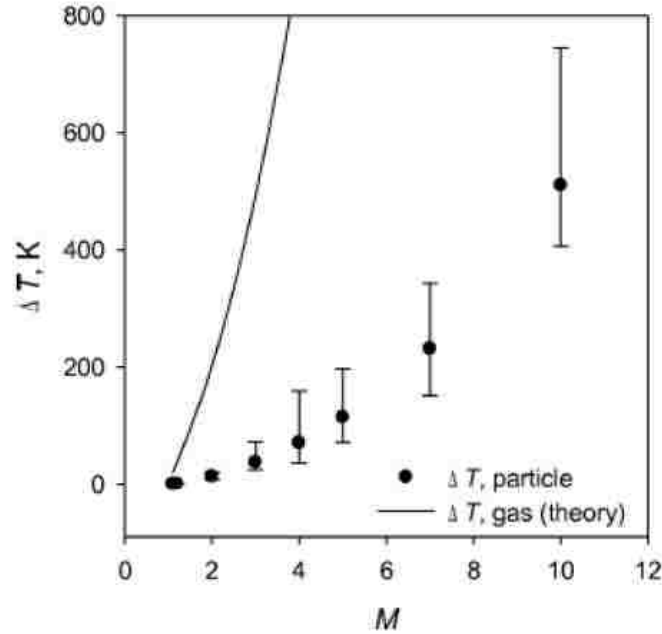
Figure 2.5: Increase of temperature in a 500 nm diameter spherical particle as the result of shock passage in a shock tube. The particle is assumed to have the same thermodynamic properties as water. Solid curve indicates temperature rise in air behind the shock.

temperature change of air behind a shock wave vs. the Mach number. This temperature rise is assumed to occur instantaneously with the shock passage. The symbols represent the temperature rise of particles surrounded by air at T_2, as given by Eq. 2.15. The time interval between the shock passage and the arrival of the expansion fan that cools the air surrounding the particles was calculated using the Gas Dynamics Calculator, and was typically on the order of milliseconds. Particles are

assumed to be 500 nm diameter spheres with thermodynamic properties of water. An iterative variation of the lumped capacitance solution, Eq. 2.14, was used with a decaying convection coefficient when calculating Bi, in Eq. 2.10. The properties of the surrounding air were assumed to remain constant until the arrival of the rarefaction wave fan. Some of the table data for the thermodynamic properties had to be extrapolated, thus introducing uncertainties shown as error bars.

The effects of forced convection decline as v_p is accelerated to equal v_g, in accordance with Eq. 2.8, thus the local convection coefficient decreases with time [14]. For Mach 4 the temperature rise is approximately 40 K where at least some bioagent neutralization may be expected to occur (steak done to this temperature would be medium rare). The temperature rise is significantly larger at higher Mach numbers, which would increase the probability of bioagent defeat.

2.4   Summary

Many assumptions have been made to represent particle interaction with shock driven flows. Particle clumping from gas density increases may neutralize the threat of suspended bioagents by reducing their ability to stay airborne. Rapid acceleration from shock accelerated flow may impact suspended bioagents with a force great enough to neutralize them. The lumped capacitance method with decaying convection coefficient can be used to predict the heating of a suspended particle in a shocked flow. This temperature rise may lead to bioagent defeat. These results require further experimentation to confirm the findings.

Chapter 3

Shock Experiment Setup

3.1   Shock Tube Facility

The shock tube facility was designed to meet functional requirements that it safely operate at Mach 4 and be tiltable to any angle. The design began by decomposing the overall shock tube into sections which make it possible to assign roles for each component. The shock tube, shown in Fig. 3.1 is comprised of four modular sections, which are referred to as follows:

1. Driver section

2. Driven section

3. Test section

4. Run-off section

Each section of the shock tube was fabricated with flanges on each end. The shock tube is assembled by bolting the flanges together; the assembled length of the shock tube is 5.8 m. A Mylar diaphragm is placed between the driver and driven sections. The test section is represented with a different shading because it is currently made
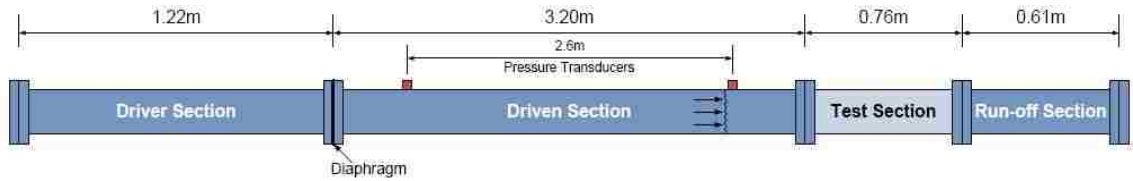
Figure 3.1: Shock tube schematic showing lengths, as well as diaphragm and transducer locations.

from transparent polycarbonate, while the other three are made from aluminum. The test section will later be constructed from aluminum with laser-quality glass windows. Two pressure transducers, which sense transient pressure changes, are mounted to the top of the driven section 2.6 m apart. The signals from these devices produce pressure traces which are used to calculate the shock wave velocity. The shock wave travels from left to right, and the run-off section can be capped or left open to the atmosphere. Capping the shock tube causes the shock wave to reflect back into the flow, allowing for study of shock focusing.

The role of the driver section is to initially maintain a higher pressure than the rest of the shock tube. The driver gas is injected and contained in the driver section at a constant pressure. The driver section is sealed off from the driven section by the Mylar diaphragm and may be pressurized with an inert gas such as air, helium, or nitrogen. The shock wave velocity is a function of temperature, density, and pressure. Since varying the temperature of the gases is challenging, the pressure, and thus density, of the driver gas is the most convenient means of adjusting the shock wave speed.

The *Gas Dynamics Calculator* [15], provided by the Wisconsin Shock Tube Laboratory, calls for inputs of desired Mach number, initial driven gas pressure and temperature, and driven gas temperature; and outputs the shock wave pressure, temperature, density, sound speed, and velocity. Another important output of this calculation is initial driver gas pressure. This value reveals how much pressure the driver section must safely withstand.
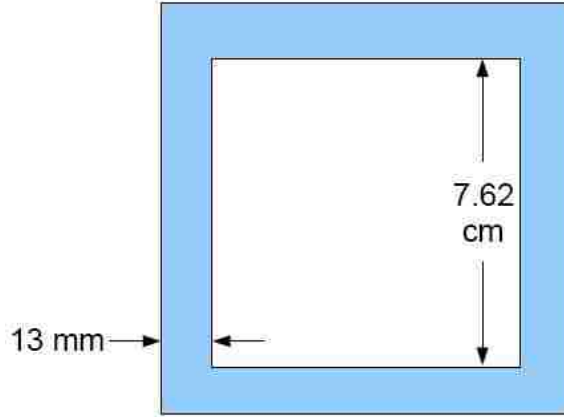
Figure 3.2: Cross-section dimensions of the square tube selected for the shock tube.

Safety is the primary consideration in the design of pressure vessels, such as the driver section. According to the *Pressure Vessel Handbook* [16], the maximum allowable working pressure is the internal pressure at which the weakest element of the vessel is loaded to the ultimate permissible point, and is determined by the driver section geometry. Pressure vessels that are intended for continuous use are designed with a factor of safety (FOS) of at least 3.5 [16]. The factor of safety is

$$FOS = \frac{\sigma_Y}{\sigma_{allow}} \tag{3.1}$$

where σ_Y is the yield stress and σ_{allow} is the allowable stress if the material. Finite element analysis (FEA) software was used to determine the stresses in an internally loaded tube. The FEA software package chosen was *ABAQUS* [17].

The tube geometries considered were limited to those readily available for procurement, thus eliminating the need for extensive custom fabrication. The preliminary design of the driver section assumed a tube of square cross-section, with internal sides of 7.62 *cm* and wall thickness of 13 *mm*, as shown in Fig. 3.2. For aluminum alloy 6061-T6 as the material for the driver section, $\sigma_Y = 276 \; MPa$. The software reveals that in order to achieve a FOS of at least 3.5, the internal pressure of the square aluminum tube must not exceed 3.5 *MPa*.
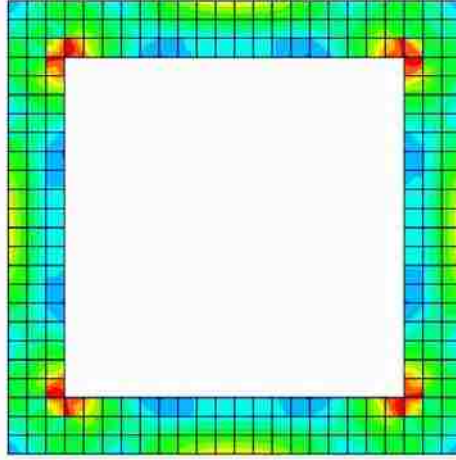
Figure 3.3: Analysis results of square cross-section driver section showing the stress concentrations at the inside corners [17].

To produce a shock wave in air of Mach 4, with helium as the driver gas, the *Gas Dynamics Calculator* computes that an initial driver gas pressure of approximately 13.8 MPa is required. These levels exceed the maximum allowable pressure for the square driver section design. The maximum pressure of 3.5 MPa will produce a shock wave of Mach 2.9, falling short of the Mach 4 requirement. The square tube design does not offer the strength needed because stress concentrations develop at the internal corners of the tube, as shown in Fig. 3.3. The regions shaded red indicate these as the failure points.

It was decided to use a round cross-section tube for only the driver section, thus eliminating all stress concentrations. The tube cross-section chosen for the driver section is 10 cm outer diameter with 9.5 mm wall thickness, giving 8.1 cm inner diameter, as shown in Fig. 3.4. The round tube section is assumed to be a thick-walled cylinder [18], and thus the stress in the circumferential direction, or hoop stress, σ_c, at any distance on the wall radius, r, is

$$\sigma_c = \frac{p_i r_i^2 - p_o r_o^2}{r_o^2 - r_i^2} - \frac{r_i^2 r_o^2 (p_o - p_i)}{r^2 (r_o^2 - r_i^2)} \tag{3.2}$$
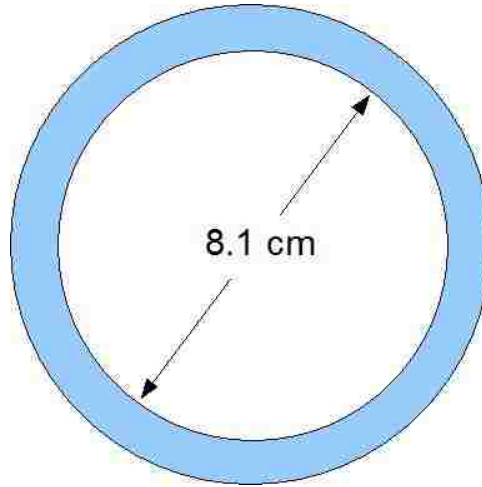
Figure 3.4: Round cross-section tube selected for the driver section.

where p_i is internal pressure, p_o is external pressure, r_i is inner tube radius, and r_o is outer tube radius. The hoop stress for a cylindrical pressure vessel is maximum at the inner wall, $r = 4.05$ cm. The resulting hoop stress from Eq. 3.2 where $p_i = 13.8$ MPa is $\sigma_c = 66.5$ MPa. From Eq. 3.1 the $FOS = 4.1$, meeting the safety requirement for pressure vessel design.

The final driver section length is 1.22 m, round aluminum 6061-T6 tube, with 10 cm outside diameter and 9.5 mm wall thickness. The mass of the selected driver section tube is 9.1 kg, and the total internal volume of the driver section is 0.027 m^3. This piece was purchased locally, but a manufacturing defect was found. The original round tube was non-concentric in that the inside diameter did not have the same center axis as the outside. This defective piece was returned and a conforming tube was successfully delivered.

To facilitate the tiltable requirement the shock tube will be mounted to an aluminum I-beam structure. The support structure adds strength to the shock tube and negates deflection of the tube under its own weight.

After each test it is necessary to prepare for the next shot, which includes replacing the ruptured diaphragm with a new one and resetting the puncturer. This
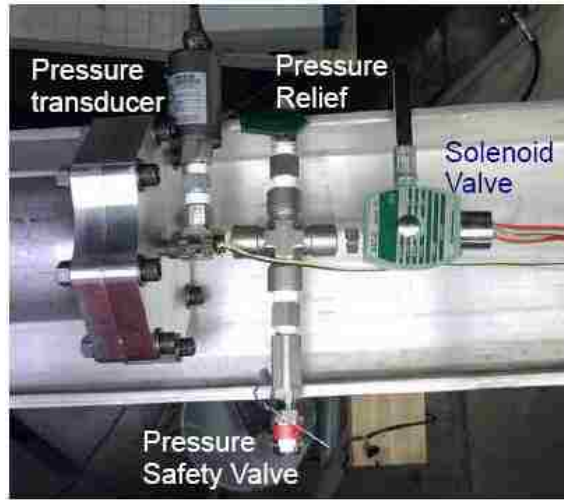
Figure 3.5: Driver gas injection system.

is accomplished by laying the driver section on a C-channel aluminum beam, which is mounted coplanar with the I-beam. Having the driver section on this structure makes replacing the diaphragm a trivial matter of unbolting the driver section and sliding it back.

The gas injection system for the driver section includes an electric solenoid valve, a pressure sensor, and a safety relief valve. These three components are attached through a cross-fitting and a T-fitting, as shown in Fig. 3.5. The T-fitting threads into the end cap of the driver section. Driver gas is supplied by a cylinder of Helium that passes through the solenoid valve. The valve is opened to allow gas to flow, pressurizing the driver section, and then closed to stop the flow. The valve is normally closed without power. The valve is wired through a switch that supplies 110 VAC and opens when the manual control toggle switch is closed. A spring loaded pressure safety relief valve is installed on the injection system. In the event the pressure inside the driver section exceeds a predetermined pressure the valve opens to reduce the tube pressure. The pressure safety valve has been preset to 6.9 MPa, and will require adjustment when higher pressure is required in the driver section. The digital pressure sensor is used to monitor the driver gas pressure loading in the driver section.
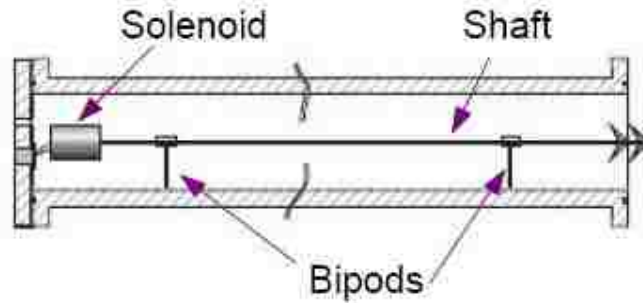
Figure 3.6: The puncture device system. Shown is the razor-tipped shaft that ruptures the diaphragm, the supporting bipods, and the puncture solenoid.

Currently a Fluke multimeter monitors the voltage reading from the pressure sensor. The voltage measurements are calibrated to correlate with voltage readings from pressure values inside the driver section. The table created as a reference to the voltage corresponding to pressure and the resulting Mach number for helium driver gas is shown in Fig. A.1.

The puncture device system is also mounted to the driver section end cap. The puncture system includes an electric solenoid, steel shaft, two bipod linear bearings, and a razor tip. The schematic of the puncture system is shown in Fig. 3.6. Threaded aluminum standoffs firmly mount the solenoid to the end cap. Power is supplied to the solenoid, which is inside the sealed volume, by a hermetically sealed feed-through connector. The connector is thread mounted to the end cap flange and soldered to two wires, a power wire and return. The solenoid is wired through a push button switch, which is the fire signal to the system. The solenoid transfers an axial impulse motion to a long steel shaft, which is supported by Teflon®-coated linear bearings, which were pressed into custom brass bushings. Two steel dowels were pressed in to the brass bushings 60° apart. The result is a bipod which keeps the puncture shaft coaxial with the driver section. The shaft is tipped with a four blade arrowhead that form an ×. The arrowhead was fabricated from heavy-duty utility blades. The blades puncture the diaphragm uniformly from the center to the corners of the driven section, allowing the full expansion of the driven gas into the driven section

with minimal blockage.

Driven Section

The selected driven section is made from a 6061-T6 square aluminum tube, with inner wall dimensions 7.62 *cm* × 7.62 *cm*, and 13 *mm* thick walls, as shown in Fig. 3.2. This is the same tube originally selected for the driver section. The driven section is 3.2*m* long. Similar to the driver section, the driven section is internally loaded once the diaphragm is ruptured, however the loads are instantaneous and not as large as in the driver section. The total shock tube volume is large. Thus even when the shock tube end is capped, the final pressure is just a fraction of the initial driver gas pressure. These assumptions allow for confidence that the driven section will not experience loads beyond safe levels.

The support structure described above is used to support the weight of the driven section and allow for tilting. Two Omega pressure transducers are flush mounted to the top inside surface of the driven section. The transducers are made flush to the driven section top inside surface by custom-made brass spacers. The spacers have internal threads that match the external threads of the pressure transducers. The spacers are epoxied to the outside top of the tube and the transducers thread snuggly into place. These transducers are designed to sense impulsive pressure changes and are ideal for use on the shock tube. They are mounted 2.6 *m* apart and collect data that reveals the shock wave velocity. Their more important role will be triggering the diagnostics system. Signals from the pressure transducers are routed to a signal delay generator that fires the high-speed camera, and will eventually trigger laser pulses for PLIF and PIV studies.
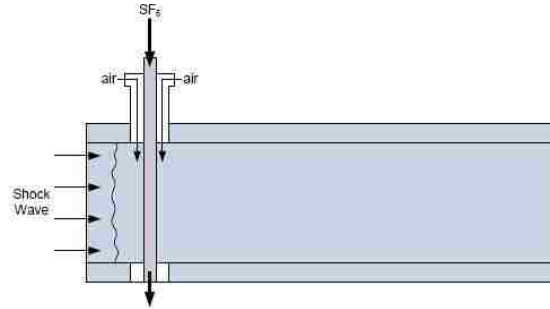
Figure 3.7: The test section showing the co-flow heavy gas cylinder injection system at 0°.

Test Section

The test section has the same cross-section dimensions as the driven section shown in Fig. 3.2. The test section was constructed from four 13 mm thick, 0.76 m long, Lexan® polycarbonate sheets. The sheet were joined with adhesive and screws, forming a square tube. The Lexan® polycarbonate is an ideal material because the test section needs to be transparent but able to sustain many shock wave tests. The test section mounts to the driven section with flanges attached to each end. The flanges are fastened to the test section with eight screws, but the softness of the polycarbonate caused the threads to strip and the flanges fell off. To alleviate this issue, two threaded rods compress the test section between the driven and run-off sections. The first test section assembly shattered under the stress of the shock wave because of excessive compressive preloading in the polycarbonate tube caused by over-torquing the threaded rods. This problem was solved by only hand tightening the nuts on the threaded rods.

The test section has an injection hole on the top and an exhaust hole on the bottom. A heavy gas, SF_6, is fed into this hole and allowed to flow through the section and out the bottom, as shown in Fig. 3.7. The SF_6 cylinder always feeds normal to the ground so multiple test sections with different angle holes are needed when the shock tube is tilted. Currently there are two different test sections, one is
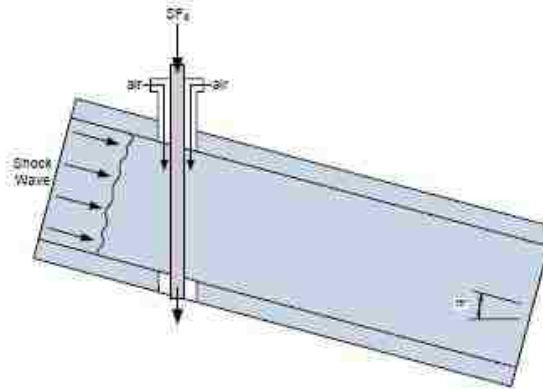
Figure 3.8: The test section showing the co-flow heavy gas cylinder injection system at 15°.

for a vertical column for 0° experiments, and another for 15° experiments, as shown in Fig. 3.8. The SF_6 gas along with glycol droplets from a fog machine feed into the test section in a gravity-driven flow.

The heavy gas mixture comes from a 20 gallon glass tank positioned higher than the test section. The SF_6 reaches the tank by traveling from a gas cylinder into a filtering flask. This filtering flask will later be used to infuse the gas with acetone for PLIF and PIV diagnostics. From the flask, the gas flows into the top of the tank where a barbed hose connector is mounted.

A Stallion fog generator positioned directly atop the tank directs fog into the tank through a 90° elbow. The fog contains glycol droplets which mix with the SF_6. A hose attached to the base of the tank carries the mixture into the test section. The flow of the gas into the test section is controlled by a ball valve on the hose. The valve is kept closed to prevent the heavy gas in the tank from escaping until a test is run.

Early problems with the initial conditions of the gas cylinder were attributed to heat added to the gas by the fog generator. This issue was addressed by placing a bucket of ice inside the tank during initial setup. The fog is cooled as it enters the
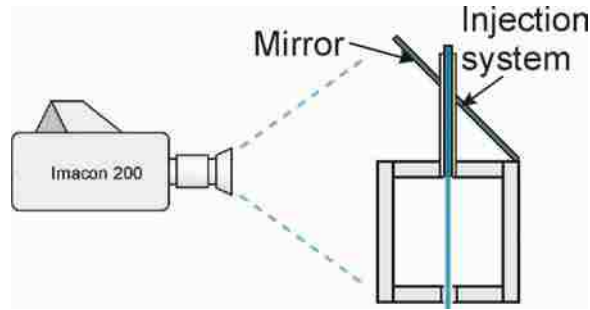
Figure 3.9: Schematic of the test section with the mirror positioned for visible light Mie scattering visualization.

tank and heating of the heavy gas mixture is minimized.

A mirror is mounted at a 45° angle above the test section, as shown in Fig. 3.9. This allows the camera to capture the shock interaction with the gas cylinder both from the side and from above. The test section is illuminated by two flood lights and four grid arrays of 400 LEDs. Initial conditions can be affected by heat generated from the flood lights, so they are turned on shortly before each test.

The initial conditions were found to be unstable for a simple SF_6 cylinder passing through the test section. To address this a concentric tube feeds low pressure air around the SF_6 cylinder. This co-flow device eliminates the shear layer between flowing SF_6 and air in the test section, producing laminar initial conditions [8].

Flanges

The flanges are the backbone of this apparatus and allow the connection of all sections together in different configurations. Each flange was made from 0.75 in thick aluminum plate. The flanges have a 6 in circular bolt pattern containing eight equally-spaced through holes to accommodate standard $3/8in$ bolt hardware. Another common feature is a 0.125 in circular groove which seats a 4 in diameter O-ring, serving as a pressure seal. The flanges were precision CNC machined in the University of New Mexico student machine shop. A counter bore was incorporated

Figure 3.10: (left)Aluminum plate used to fabricate shock tube with stock material bolted to a CNC machine. (right)Completed flanges, fabricated in the UNM student machine shop.

to ease the assembly of the flange to tube ends. The flanges were aerospace grade welded to the tube sections by BJ Welding Service in Albuquerque.

3.2 Diagnostics System

The diagnostic system thus far includes two pressure transducers, a signal delay generator, an ultra high-speed camera, and a data acquisition unit.

High-Speed Camera

The key diagnostic tool is the DRS Imacon 200, shown in Fig. 3.11. The Imacon 200 is the most advanced and sophisticated ultra-high speed digital imaging system in the world [19]. The imaging system is based on multiples of intensified CCD modules. The camera has high spatial and temporal accuracy and flexible software operation providing a versatile recording system ideally suited for ultra fast events, such as shock wave studies. The camera is capable of capturing 14 frames with programmable framing rates from 1000 to 200 million frames per second [19]. The camera uses a Nikon Bayonet F style lens mount, which allows for a variety of lenses,

microscopes and custom optical applications. The camera will be used extensively to capture shock wave interactions through Mie scattering imaging, as well as using PLIF and PIV techniques.

Figure 3.11: DRS Imacon 200 ultra-high speed camera, captures 14 frames from 1000 to 200 million frames-per-second [19].

Data Acquisition System

Shock tube experimental data is acquired both as image data and pressure trace data. The 14 images are sequentially captured by the high-speed camera and stored on a connected computer. Two pressure transducers send voltage readings to a signal delay generator. Larger voltage from the transducer corresponds to larger pressure inside the shock tube. The delay on the generator is preset for the Mach number of the experiment being conducted. The signal generator then sends fire commands to the camera, and for PLIF and PIV, to three lasers, as shown in Fig. 3.12. In addition to triggering the camera, the pressure transducer voltage signals are recorded on a National Instruments PXI chassis. The PXI chassis has an oscilloscope program which triggers and captures the reading from the pressure transducers. These signals are the pressure trace data which give validation of the shock wave velocity.
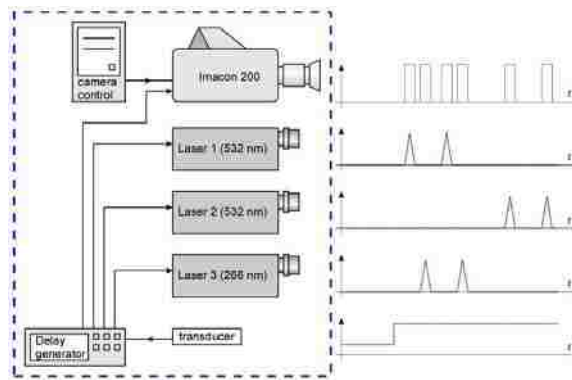
Figure 3.12: Image data acquisition scheme.

Chapter 4

Shock Tube Performance

4.1 Preliminary Image Data

The Imacon 200 camera is positioned to capture the Richtmyer-Meshkov instability (RMI) resulting from shock wave gas cylinder interaction from both side and top, as shown in Fig. 4.1. The image on the right shows the boundaries of concern, which are shown in a dotted box. In the side view, a indicates the gas cylinder, while b indicates the same gas cylinder cross-section from above.

Figure 4.1: (left)Imacon 200 camera setup to capture RMI in the test section; (right)the top view and side view of the test section.

Twelve horizontal shock study frames are shown in Fig. 4.2. Although fourteen

Figure 4.2: Processed image sequence, inverted and contrast-enhanced, *Mach* 2 acceleration of SF_6 gas cylinder with shock tube angle of 0°.

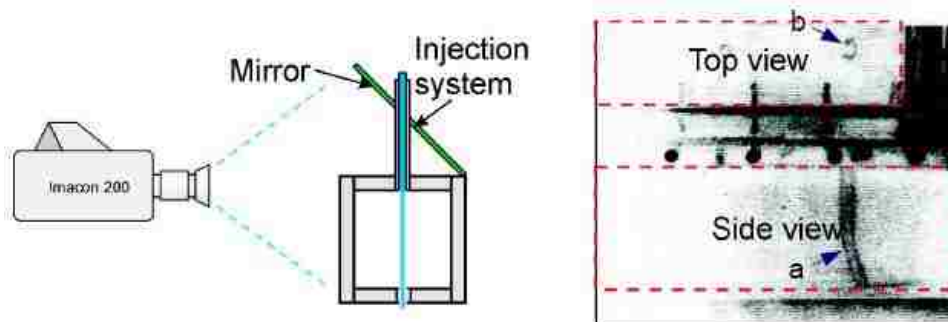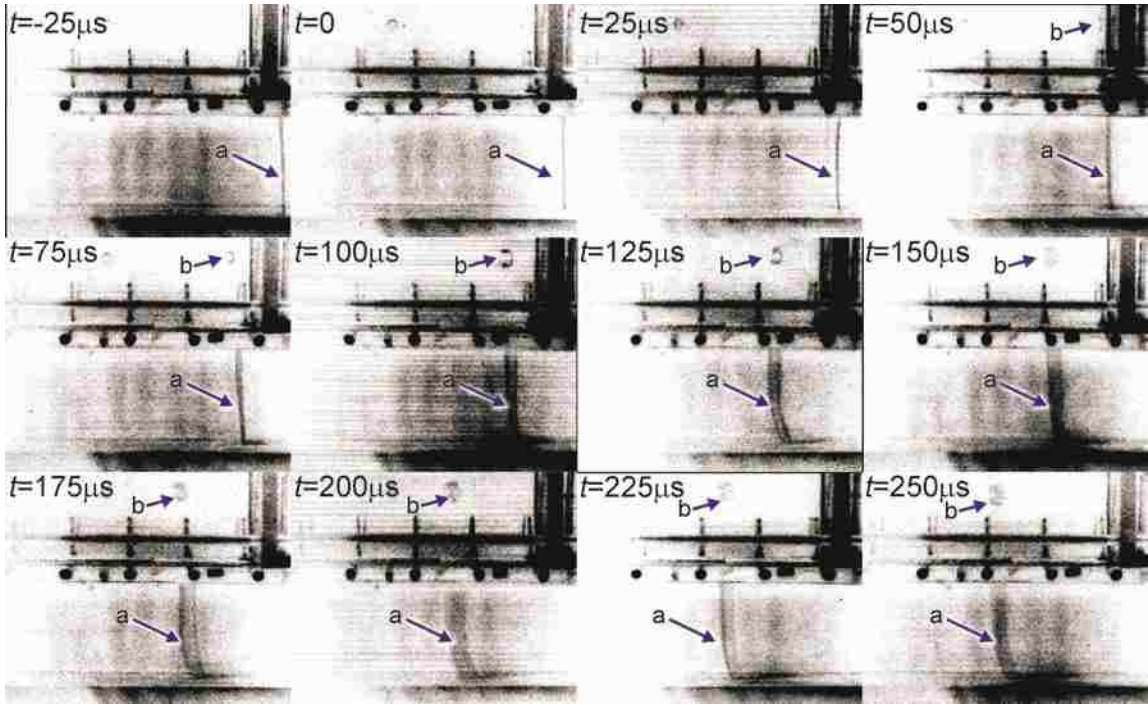images were captured, the last two are omitted. The first frame is labeled $t = -25\,\mu s$, and arrow a is indicating the initial conditions; this is just before the shock wave arrives. The top view of the initial gas cylinder is not visible because it is obstructed by the gas injection system. The shock wave arrives at $t = 0$. The cylinder of SF_6 with glycol droplets begins to move to the left as the shock wave passes. The velocity of the gas cylinder is the piston velocity of the flow behind the shock wave. The top view at $t = 100\,\mu s$ clearly shows the formation of the counter rotating vortex pair characteristic of RMI.

Oblique shock wave study requires that the shock tube be tilted, either by raising the driver section higher than the test section or the reverse. The shock tube has been tested with the driver section tilted 15° above the test section. Images from a Mach 2, 15° oblique shock study are shown in Fig. 4.3. Although fourteen frames were captured during this experiment, frames 1-4 and 13-14 are omitted. The initial

conditions, a, for the 15° oblique shot are shown at $t = -75, -50, -25$ μs. Note that the cylinder of SF_6 seeded with glycol droplets appears to be oriented at 15° with respect to vertical. However, the heavy gas cylinder is actually vertical, since it is gravity-driven flow, and the camera is tilted with the test section. Once again, the top view of the initial heavy gas cylinder is not visible because of the injection system. At $t = 0$ μs the shock wave passes through the cylinder of SF_6 seeded with glycol droplets causing motion to the left. At $t = 25$ μs the top view of the gas cylinder enters the viewable region. The counter rotating vortex pairs are not visible in the top view under Mie scattering conditions, but the addition of advanced techniques, such as PLIF and PIV, will allow any cross-section of the SF_6 cylinder to be highlighted.

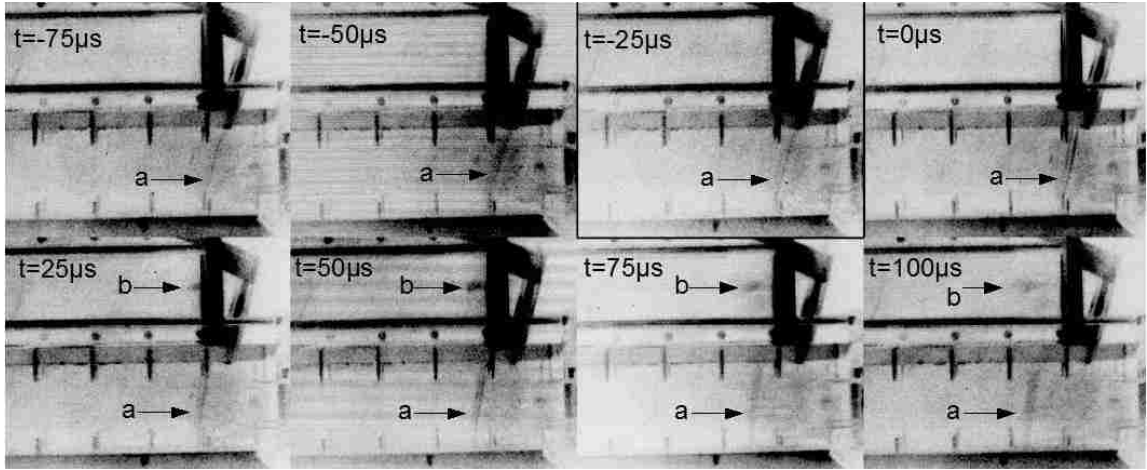Figure 4.3: Processed image sequence, inverted and contrast-enhanced, Mach 2 acceleration of SF_6 gas cylinder with shock tube angle of 15°.

4.2 Shock Tube Calibration

Benchmarking the shock tube results against theoretical expectations is important for reliable and repeatable shock tube experiments. The shock wave velocities naturally vary from shot to shot. These variances can be attributed to diaphragm material

quality, puncture device operation, and temperature. The theoretical Mach number for each shot is determined using the *Gas Dynamics Calculator* [15]. Measured quantities provide the actual Mach number of each shot. Pressure transducer data was used to determine shock velocity and thus the actual Mach number. The shock tube has thus far been tested for Mach number Mach 1.2, 1.9, and 2.4. Inputs to the *Gas Dynamics Calculator* are: driver gas = helium, driven gas = air, initial driven section pressure = 83.4 kPa, and temperature = 295 K. The driver pressures from the *Gas Dynamics Calculator* to produce Mach 1.2, 1.9, and 2.4 are 0.175, 0.788, and 1.798 MPa, respectively.

The pressure traces shown in Fig. 4.4 describe the moment the shock wave passes each pressure transducer in the driven section. The time in seconds between spikes

Figure 4.4: Actual pressure trace data for theoretical Mach 1.2 shock wave. The actual shock wave speed indicates Mach 1.29.

in the two pressure traces indicates how long it takes the shock wave to travel from pressure transducer 1 to transducer 2. The pressure transducers are 2.6 m apart, and dividing this distance by the time difference yields the shock wave speed. In Fig. 4.4, there is 6.0 ms between the peaks of the two trigger pulses, corresponding to a shock wave speed of 433 m/s or Mach 1.29. The measured result is 7.5% greater

than the theoretical value.

Pressure trace data for Mach 1.9 is shown in Fig. 4.5. The time difference
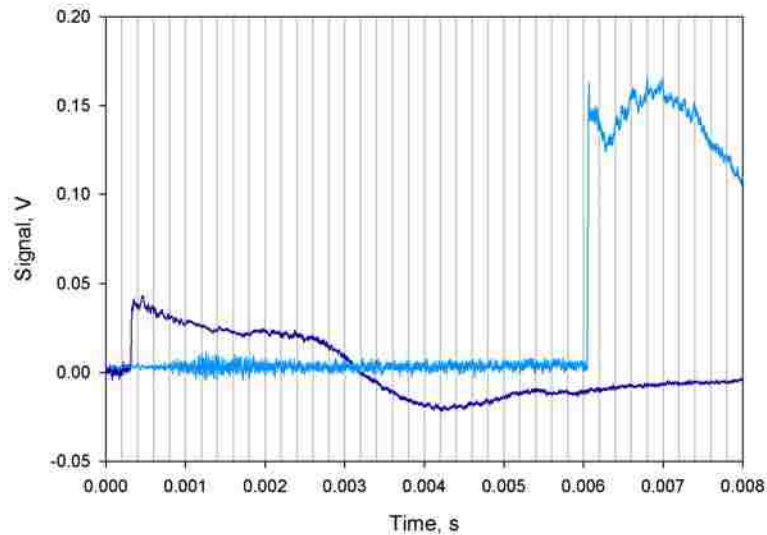

Figure 4.5: Actual pressure trace data for theoretical Mach 1.9 shock wave. The actual shock wave speed indicates Mach 2.05.

between the largest pulses in each of the two pressure transducers is 3.8 ms. This corresponds to an actual shock wave speed of 684 m/s or Mach 2.05. The actual shock wave speed is 7.9% greater than the theoretical Mach number. The errors for Mach 1.2 and 1.9 shots are similar.

Finally, pressure trace data for Mach 2.4 is shown in Fig. 4.6. The time difference between the maximum peaks is 3.4 ms corresponding to an actual shock wave speed of 765 m/s or Mach 2.29. Here the actual Mach number is 4.6% less than the theoretical value. The error for Mach 2.4 is less than that at lower Mach numbers, so higher driver pressures produce actual results closer to theoretical. The actual shock wave speed is less than theoretical, although further investigation is needed to determine if this is aways the case.
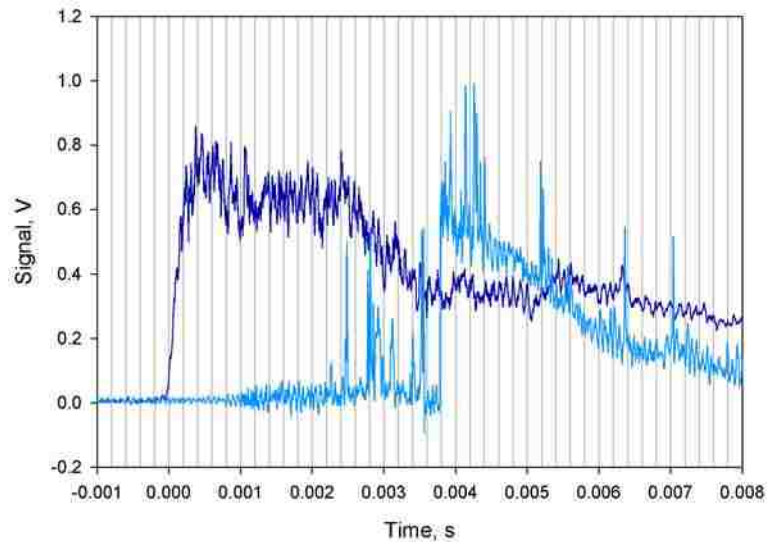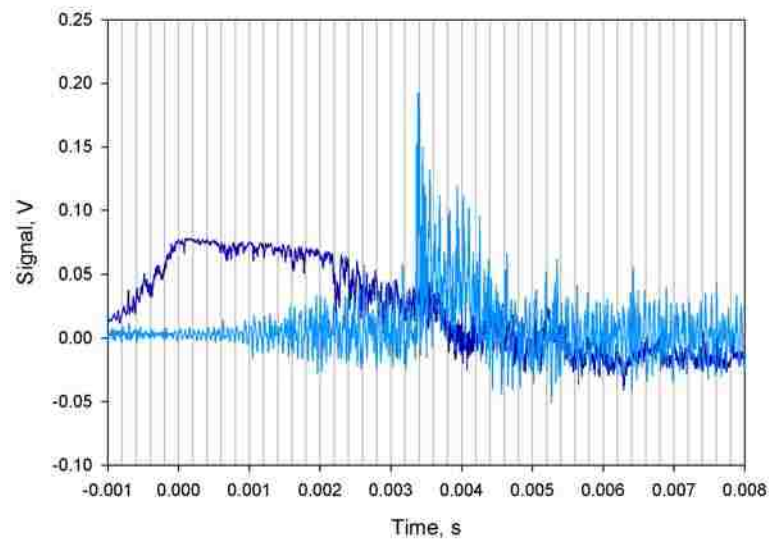
Figure 4.6: Actual pressure trace data for theoretical Mach 2.4 shock wave. The actual shock wave speed indicates Mach 2.29.

Chapter 5

Conclusions

Benchmarking capabilities have been limited by experimental deficiencies which are attributed to the challenge of developing appropriate experimental capabilities. A novel shock tube facility has been constructed which addresses the need to test strong shock wave interactions. This facility may be used to explore the lethal effects of strong shock wave acceleration on airborne bioagents. Shock waves interact with bioagents by heating, acceleration, and compression. This theoretical study shows that shock waves greater than Mach 4 can neutralize bioagent threats. Calibrating the shock tube reveals that the tube can produce strong shock waves and has been tested up to Mach 2.4. Data from testing reveals that shock tube results are in good agreement with theoretically computed parameters.

Higher Mach numbers can be achieved through shock focusing, where the reflection of the shock wave is studied. The shock tube is 5.8 m long because the driver section allows the shock front to fully form and the run-off section allows shock interactions with heavy gas and particles to take place in front of the camera before the reflected incident wave returns. The experimental shock speeds are slightly larger than the theoretical because temperatures in the lab or in the driver section may differ from what was entered into the *Gas Dynamics Calculator* [15].

5.1   Future Work

The test section will be fitted with 266 *nm* laser glass windows for use with PLIF and PIV diagnostic techniques. Experiments with interactions at different angles will provide further benchmarking. Investigations will be conducted with benign bacterial spores. A new shock tube test control box will be fabricated. New LabVIEW® test control software will be created to enable automated experiments. The shock tube will be a lasting tool for the study of physical gas dynamics phenomenon.

Analysis of the planar and oblique shock wave interactions with the SF_6 seeded with glycol droplets is being conducted by E.P. Johnson [20]. Preliminary results show that baroclinic vorticity in 3-D does play a role in the rotation of the gas cylinder in the vertical plane parallel to the streamwise direction. More experiments will be conducted to further the understanding of oblique shock interactions with a heavy gas cylinder.

Appendix A

Driver section voltage-pressure correlations

Mach	Pressure,Mpa	Pressure,psi	Voltage,V
1.0	0.097	14	0.077
1.1	0.132	19	0.106
1.2	0.175	25	0.140
1.3	0.227	33	0.181
1.4	0.288	42	0.230
1.5	0.362	52	0.287
1.6	0.444	64	0.354
1.7	0.542	79	0.433
1.8	0.656	95	0.523
1.9	0.788	114	0.628
2.0	0.939	136	0.749
2.1	1.113	161	0.888
2.2	1.312	190	1.046
2.3	1.539	223	1.228
2.4	1.798	261	1.435
2.5	2.094	304	1.670
2.6	2.430	352	1.938
2.7	2.811	408	2.243
2.8	3.245	471	2.588
2.9	3.736	542	2.980
3.0	4.294	623	3.425
3.1	4.925	714	3.929
3.2	5.640	818	4.499
3.3	6.450	936	5.145
3.4	7.367	1069	5.877
3.5	8.408	1219	6.705
3.6	9.583	1390	7.644
3.7	10.914	1583	8.706
3.8	12.423	1802	9.910
3.9	14.133	2050	11.274
4.0	16.072	2331	12.821
4.1	18.272	2650	14.575
4.2	20.768	3012	16.567
4.4	26.827	3891	21.400
4.6	34.670	5028	27.656
4.8	44.859	6506	35.785
5.0	58.158	8435	46.391

Figure A.1: Driver pressure required to achieve the desired Mach number. Multimeter voltage from the driver pressure gage is also shown.

Appendix B

Matlab code for bioagent defeat study

```
%AccelEffects.m uses Matlab to calculate the acceleration
%effects of the shock wave on a particle.
function AccelEffects
g=1.4; %gas constant
C=120;      %Sutherland's Constant, K
T1=291.15;  %room temperature in lab, K
p1=83400;   %atmospheric pressure, Pa
r1=1;       %density of air in the lab, kg/m^3
rp=998;     %density of particle (used water), kg/m^3
d=500e-6;   %particle diameter, m
%Presize Arrays
Tjmp=zeros(21,1); T2=zeros(21,1); u=zeros(21,1);
m=zeros(21,1); du=zeros(21,1);
M=[1.0:.2:5]';
for i=1:21
    Tjmp(i,1)=((1+((g-1)/2).*M(i,1)^2).*((2.*g/(g-1)).*M(i,1)^2-1))/
```

```
        (((((g+1)^2)/(2.*(g-1))).*M(i,1)^2);
    T2(i,1)=T1.*Tjmp(i,1);  %Temperature accross the shock in Kelvin
    u(i,1)=330.*M(i,1);      %Shock velociy, m/s
    m(i,1)=(18.27e-6).*((T1+C)./(T2(i,1)+C)).*(T2(i,1)./T1)^(3/2);
                          %Dynamic viscosity of air
    du(i,1)=u(i,1).*(18./(d)^2).*(m(i,1)./rp).*9.81^-1;
                          %Particle Acceleration, 10^1 g
end
Tjmp;T2;m;du;
scatter(M,du,'filled')
xlabel('M') %('Mach number')
ylabel('Particle Acceleration, g')
```

Appendix C

Test Procedure

The following procedure instructs the user how to use the shock tube in its simplest form. It is anticipated that the operation of the shock tube will become computer controlled. However please follow these steps for safe and successful shock tube experiments:

1. Place a bucket of ice in the SF_6 reservoir and replace the tank lid.

2. Place the fog generator above the tank and turn on the power.

3. Begin the the SF_6 flow at approximately 15 ft^3/min.

4. Unbolt the driver section and install an unruptured diaphragm.

5. Test the SF_6 level by injecting small amounts of fog into the tank.

6. Inject large amounts of fog into the tank when the SF_6 tank is at least half full.

7. Open the valve allowing the SF_6 to flow into the test section.

8. Power on the additional lighting.

9. Arm the high-speed camera and the data acquisition system.

10. Refer to Fig. A.1 to determine the pressure and voltage reading related to the desired Mach number.

11. Open the solenoid valve on the driver gas injection system; the valve will hum when open.

12. Slowly turn the regulator on the helium tank letting the gas flow into the driver section.

13. Stop increasing the pressure form the helium tank when the voltage reading on the multimeter reads the desired voltage.

14. Close the solenoid valve, the shock tube is ready of fire. **Caution:** Earplugs should be worn at this point.

15. Press the button to activate the puncture device.

16. Ensure the diagnostics functioned correctly, the pressure traces should be displayed and the camera should have fired.

17. Reduce the pressure to zero on the helium regulator, and close the helium tank valve.

18. Open the pressure relief valve on the regulator to purge the gas line.

19. Save the pressure trace data.

20. Save the camera images and the video.

References

[1] G. Taylor. The instability of liquid surfaces when accelerated in a direction perpendicular to their planes. *Proceedings of the Royal Society of London. Series A, Mathematical and Physical Sciences*, 201:192–196, 1950.

[2] R.D. Richtmyer. Taylor instability in shock acceleration of compressible fluids. *Communications on Pure and Applied Mathematics*, 8:297–319, 1960.

[3] M. Brouillette. The Richtmyer-Meshkov instability. *Annual Review of Fluid Mechanics*, 34:445–468, 2002.

[4] T.V. Inglesby, D.A. Henderson, J.G. Bartlett, M.S. Ascher, E. Eitzen, A.M. Friedlander, J. Hauer, J. McDade, M.T. Osterholm, T. OToole, G. Parker, T.M. Perl, P.K. Russell, and K. Tonat. Anthrax as a biological weapon: Medical and public health management. *The Journal of the American Medical Association*, 281(18):1735–1745, May 1999.

[5] A.D. Pannifer, T.Y. Wong, R. Schwarzenbacher, M. Renatus, C. Petosa, J. Bienkowska, D.B Lacy, R.J. Collier, S. Park, S.H. Leppla, P. Hanna, and R.C. Liddington. Crystal structure of the anthrax lethal factor. *Nature*, 414:229–233, November 2001.

[6] R.D. Zucker and O. Biblarz. *Fundamentals of Gas Dynamics*. John Wiley & Sons, Inc., 2nd edition, 2002.

[7] L.D. Landau and E.M. Lifshitz. *Fluid Mechanics*. Butterworth-Heinemann, 2nd edition, 1987.

[8] G. Orlicz. Shock driven instabilities in a varicose, heavy-gas curtain: Mach number effects. Master's thesis, The University of New Mexico, December 2007.

[9] S. Kumar, G. Orlicz, C. Tomkins, C. Goodenough, K. Prestridge, P. Vorobieff, and R. Benjamin. Stretching of material lines in shock-accelerated gaseous flows. *Physics of Fluids*, 17(8):082107, 2005.

References

[10] S. Kumar, P. Vorobieff, G. Orlicz, A. Palekar, C. Tomkins, C. Goodenough, M. Marr-Lyon, K.P. Prestridge, and R.F. Benjamin. Complex flow morphologies in shock-accelerated gaseous flows. *Physica D: Nonlinear Phenomena*, 235(1-2):21–28, 2007.

[11] S. Zhang, G. Peng, and N.J. Zabusky. Vortex dynamics and baroclinically forced inhomogeneous turbulence for shock-planar heavy curtain interactions. *Journal of Turbulence*, 6(N3), 2005.

[12] M.L. Chavez, P. Vorobieff, C.R. Truman, and E.P. Johnson. Experimental studies of shock wave interactions with droplets and particulates. *AIAA Paper 2009-4050*, June 2009.

[13] L.S. Fan and C. Zhu. *Principles of gas-solid flows*. Cambridge University Press, 1998.

[14] F.P. Incropera and D.P. DeWitt. *Fundamentals of Heat and Mass Transfer*. John Wiley & Sons, Inc., 5th edition, 2002.

[15] Wisconsin Shock Tube Laboratory (WiSTL). *Gas Dynamics Calculator*. The Board of Regents of the University of Wisconsin System, October 2004.

[16] E.F. Megyesy. *Pressure Vessel Handbook*. Pressure Vessel Handbook Publishing Inc., 9th edition, 1992.

[17] Dassault Systmes Simulia Corporation. ABAQUS/CAE Version 6.8-1, 2008.

[18] H.W. Haslach Jr and R.W. Armstrong. *Deformable bodies and their material behavior*. John Wiley & Sons, Inc., 2004.

[19] DRS Data & Imaging Systems, Inc., 138 Bauer Drive, Oakland, NJ 07436. *DRS's Imacon 200 Technical Specifications*.

[20] E.P. Johnson. Planar and oblique shock wave interaction with a droplet seeded gas cylinder. Master's thesis, University of New Mexico, December 2009.